Proteins with prion-like domains can form viscoelastic condensates that enable membrane remodeling and endocytosis

Louis-Philippe Bergeron-Sandoval[1], Sandeep Kumar[1], Hossein Khadivi Heris[2], Catherine Chang[3], Caitlin E. Cornell[3], Sarah L. Keller[3], Paul François[4], Adam G. Hendricks[2], Allen J. Ehrlicher[2], Rohit V. Pappu[5] and Stephen W. Michnick[1,6*]

Affiliations

[1]Département de Biochimie, Université de Montréal, C.P. 6128, Succursale centre-ville, Montréal, Québec, H3C 3J7, Canada.
[2]Department of Bioengineering, McGill University, 817 Sherbrooke St West, Room 270, Montreal, Quebec, H3A 0C3, Canada.
[3]Department of Chemistry, University of Washington, Seattle, Seattle WA 98195-1700 USA
[4]Ernest Rutherford Physics Building, McGill University, 3600 University St, Montreal, Québec, H3A 2T8
[5]Department of Biomedical Engineering and Center for Biological Systems Engineering, Washington University in St. Louis, One Brookings Drive, Campus Box 1097, St. Louis, Missouri 63130, USA.
[6]Centre Robert-Cedergren, Bio-Informatique et Génomique, Université de Montréal, C.P. 6128, Succursale centre-ville, Montréal, Québec, H3C 3J7, Canada.

*Correspondence to: S.W.M. (stephen.michnick@umontreal.ca).

Summary

Membrane invagination and vesicle formation are key steps in endocytosis and cellular trafficking. Here, we show that endocytic coat proteins with prion-like domains (PLDs) form hemispherical puncta in the budding yeast, *S. cerevisiae*. These puncta have the hallmarks of biomolecular condensates and enable membrane remodeling to drive actin-independent endocytosis. The puncta, which we refer to as endocytic condensates, form and dissolve reversibly in response to changes in temperature and solution conditions. The condensates are organized around dynamic protein-protein interaction networks, which involve interactions among PLDs with high glutamine contents. The endocytic coat protein Sla1 is at the hub of the protein-protein interaction network. Using active rheology, we indirectly characterized the material properties of endocytic

condensates. These experiments show that endocytic condensates are viscoelastic materials and allow us to estimate the interfacial tension between endocytic condensates and their surroundings. We then adapt the physics of contact mechanics, specifically the contact theory of Hertz, to develop a quantitative framework for describing how interfacial tensions among condensates, the membrane, and the cytosol can deform the plasma membrane to enable actin independent endocytosis.

Introduction

Endocytosis in eukaryotic cells can occur via two separate mechanisms. In the budding yeast *Saccharomyces cerevisiae*, membrane invagination that enables endocytosis is normally driven by growth of membrane-bound branched actin (Carlsson and Bayly 2014). A second actin independent route to endocytosis is realized when intracellular turgor pressure is reduced. This reduction of turgor pressure alleviates the tension on plasma membranes that would normally oppose membrane invagination (Aghamohammadzadeh and Ayscough 2009, Basu, Munteanu et al. 2014). In both mechanisms, endocytosis is initiated by the coordinated recruitment of a number of proteins associated with distinct stages of endocytic maturation (Kaksonen, Toret et al. 2005). Clathrin heavy and light chains first interact with initiator proteins (Ede1 and Syp1) to form a lattice on the membrane. Subsequently, early coat proteins such as Sla1, Sla2, Ent1, Ent2, and Yap1801 (Malinovska, Kroschwald et al. 2013) bind directly to the adaptor-clathrin lattice and form the cortical body (Kaksonen, Toret et al. 2005).

Electron microscopy data highlight the existence of hemispherical membraneless bodies around endocytic sites. These bodies are identifiable by following the localization of labeled endocytic coat proteins such as Sla1. The observed Sla1-labeled bodies are known to exclude ribosomes from the cytosol near the cortical sites. Importantly, these endocytic bodies form even when actin is not polymerized and the membrane is flat (Kukulski, Schorb et al. 2012). Many of the coat proteins in bodies that form around endocytic sites include prion-like domains (PLDs). These domains are intrinsically disordered, low complexity sequences that are enriched in polar amino acids such as glutamine, asparagine, glycine, and serine and are interspersed by aromatic residues such as tyrosine (Alberti, Halfmann et al. 2009, Malinovska, Kroschwald et al. 2013).

Proteins with PLDs have the ability to undergo phase separation in cells (Alberti, Saha et al. 2018) and *in vitro* (Martin, Holehouse et al. 2020) giving rise to the formation of biomolecular condensates that are mesoscale, non-stoichiometric macromolecular assemblies that concentrate biomolecules (Bergeron-Sandoval, Safaee et al. 2016, Banani, Lee et al. 2017, Powers, Holehouse et al. 2019). Here, we show that endocytosis in *S. cerevisiae* involves the concentration of PLD-containing proteins – such as the essential protein Sla1 – within biomolecular condensates that form at cortical sites. These condensates are viscoelastic, and they are scaffolded by a dense

network of PLD-containing proteins. We find that condensate formation requires an intact PLD and that the coat protein Sla1 is at the hub of the condensate driving protein-protein interaction network. The distinctive compositional biases within PLDs of coat proteins contribute to condensate formation and function. We show that the formation of the condensates and cohesiveness of molecular interactions within them, are essential for mechanoactive processes associated with actin-independent endocytosis. We present a model, motivated by the contact theory of Hertz (Hertz 1881, Derjaguin, Muller et al. 1975, Popov, Pohrt et al. 2017), to provide a plausible explanation for how interfacial tensions among condensates, the membrane, and the cytosol, can enable membrane invagination and drive actin-independent endocytosis.

Results

Sla1-labeled puncta are characterized by temperature-dependent non-covalent interactions. We sought to determine the role of PLD-containing early coat proteins in endocytosis. In the budding yeast *S. cerevisiae* we investigated actin-independent endocytosis by deleting the gene that codes for glycerol-3-phosphate dehydrogenase, a key enzyme of glycerol synthesis, (*GPD1Δ*), (Basu, Munteanu et al. 2014). Glycerol is the major osmolyte in yeast cells, and glycerol deficiency alleviates turgor pressure and tension on the membrane in *GPD1Δ* cells (*SI Appendix*, Fig. S1*A*). We could then interrogate actin-independent endocytosis in *GPD1Δ* cells by treating them with Latrunculin A (Lat A), an inhibitor of actin polymerization. The concentrations of Lat A that we use in our experiments cause a loss in localization of the filamentous actin marker Abp1 (*SI Appendix*, Fig. S1 *B-C*) (Aghamohammadzadeh, Smaczynska-de et al. 2014). We then tracked the formation and internalization of Sla1-labeled endocytic puncta at cortical sites (*SI Appendix*, Fig. S1*D*).

Proteins with PLDs and many PLDs themselves undergo reversible, thermoresponsive phase transitions with upper critical solution temperatures (UCST) in cells (Alberti, Saha et al. 2018) and *in vitro* (Martin, Holehouse et al. 2020). Systems characterized by UCST phase behavior will undergo phase separation below a critical temperature T_c and transition to one-phase homogeneous regimes above T_c (Ruff, Roberts et al. 2018). The ability of a biomolecular condensate to undergo an abrupt and reversible switch between two phases at a distinct temperature, and do so over multiple heating and cooling cycles, is a defining feature of reversible,

103 thermoresponsive phase transitions (Rayermann, Rayermann et al. 2017). Motivated by published
104 results for PLDs and proteins with PLDs, we assessed whether the Sla1-labeled endocytic puncta
105 also form and dissolve reversibly in response to increases / decreases to temperature. To investigate
106 such behavior for endocytic puncta, we quantified their sensitivity to multiple cycles of heating
107 and cooling. Sla1-labeled puncta in *GPD1Δ* cells dissolved and reassembled within seconds as the
108 temperature of the growth medium was cycled between 30˚C and 49°C (Fig. 1*A-C*). Quantification
109 of the number of puncta per cell showed a bistable response to increases / decreases in temperature
110 with an apparent transition temperature (T_t) of 45.3°C. Specifically, cells did not contain puncta
111 above T_t whereas puncta were observed in cells below T_t (Fig. 1*A, B*). Importantly, cells remained
112 viable above T_t and endocytic function was restored when the temperature dropped below T_t (*SI*
113 *Appendix*, Fig. S2*A, B*).
114
115 **Proteins are labile within endocytic condensates.** Using super-resolution fluorescence imaging, we
116 quantified the dimensions of Sla1-labeled bodies to be 209 ± 10 nm long and 118 ± 6 nm wide.
117 These inferences were based on the orientation of puncta in the imaging plane (Fig. 2*A*). Our
118 observations for top projections are similar to previous reports of Sla-labeled spherical structures
119 (Mund, van der Beek et al. 2018). They are also consistent with the electron microscopy data
120 highlighting hemispherical bodies that exclude ribosomes from the cytosol near cortical sites that
121 form in a manner that is independent of actin polymerization (Kukulski, Schorb et al. 2012).
122
123 To determine whether endocytic condensates have a characteristic mesh size, we measured the
124 diffusivity and permeability of probe molecules within and between condensates and the cytosol and at
125 endocytic sites in cells where condensates were dissolved using 1, 6-hexanediol (HD). HD has been shown
126 to dissolve a number of cellular structures, including different types of protein condensates *in vivo* (Rog,
127 Köhler et al. 2017) and *in vitro* (Alberti, Saha et al. 2018). Sla1-labeled puncta as well as those labeled with
128 all of the PLD-containing proteins that are associated with endocytic puncta, including Sla2, Ent1, Ent2,
129 Yap1801 and Yap1802 dissolve in the presence of HD (*SI Appendix*, Fig. S3*A*) (Updike, Hachey et al. 2011,
130 Kroschwald, Maharana et al. 2015). However, Syp1-mCherry, a membrane-bound endocytic initiator
131 containing a scaffold-forming F-BAR domain, was insensitive to HD (*SI Appendix*, Fig. S3*B*). This suggests
132 that membrane targeting of endocytic sites through F-BAR domain oligomerization was unperturbed by
133 HD. We also noted that HD does not disrupt membrane integrity, as monitored by membrane leakage of
134 carboxy-fluorescein (*SI Appendix*, Fig. S3 *C-E*). These results imply that HD disrupts endocytic

135 condensates and therefore, in cells treated with HD, the diffusivity and permeability of endocytic sites
136 should be identical to those of the surrounding cytosol.
137
138 We quantified the apparent mesh sizes within the endocytic puncta using Fluorescence Recovery
139 After Photobleaching (FRAP) and colocalization of FITC-conjugated dextran molecules of 2.4, 5.8 and
140 10.4 nm dimensions. The dextran probes were osmoporated into cells and FRAP was measured within
141 either Sla1- or Syp1-labeled puncta. Maintenance of cell mechanical properties following osmoporation
142 was evaluated by monitoring passive diffusion of expressed viral microNS protein nanoparticles (*SI*
143 *Appendix*, Fig. S7 *A-F*) (da Silva Pedrini, Dupont et al. 2014). Syp1 was used as a reference marker for
144 cortical patches because it was not sensitive to HD at concentrations that dissolved endocytic puncta (*SI*
145 *Appendix*, Fig. S3*B*). Although the density of the FITC-labelled 5.8 nm dextran was lower in Sla1-labeled
146 puncta than in the surrounding cytosol, the mobility of the 5.8 nm probe was equivalent in both regions
147 (Fig. 2B and *SI Appendix*, S4 *C-F*). Similarly, the fluorescence intensities of 2.4 nm and 5.8 nm FITC-
148 labelled dextran recovered equally well in the Sla1-labeled puncta and cytosolic zones (Fig. 2*B* and *SI*
149 *Appendix*, S4*F*). It is known that weakly charged molecules such as proteins do not encounter hindered
150 diffusion across phase boundaries (Münchow, Schönfeld et al. 2008). Instead, the key determinants of
151 diffusion of proteins across phase boundaries are the differential affinities to the coexisting phases and the
152 concentration gradients (Münchow, Schönfeld et al. 2008), and our data are consistent with these
153 expectations.
154
155 In contrast to the transport of 2.4 nm and 5.8 nm FITC-labelled dextran particles, only a few 10.4
156 nm dextran molecules were taken up by the endocytic puncta, although these were mobile in the cytosol
157 (Fig. 2B). Furthermore, when Sla1-labeled puncta were disrupted by HD, we observed equivalent mobility
158 of 10.4 nm FITC-labelled dextran molecules within cortical membrane sites, labelled with HD-resistant
159 protein Syp1-mCherry, and the neighboring cytosol (Fig. 2B). Our results suggest that endocytic
160 condensates are porous bodies with mesh sizes that are between 5-10 nm. These results are consistent with
161 mesh sizes of networks of proteins that engage in non-covalent physical crosslinks in biomolecular
162 condensates, and with electron microscopy data showing that endocytic puncta exclude ribosomes
163 (Kukulski, Schorb et al. 2012, Wei, Elbaum-Garfinkle et al. 2017, Alberti, Saha et al. 2018).
164
165 To measure the exchange of endocytic proteins between condensates and the cytosol, we used
166 FRAP to measure the dynamics of the coat protein Sla2. To control for dynamic Sla2 recruitment that
167 occurs early in formation of the endocytic puncta, we evaluated fluorescence recovery during periods in
168 which the apparent number of Sla2 molecules in the fluorescent foci of individual puncta was constant.

169 FRAP measurements of entirely bleached whole puncta showed signal recovery within seconds and
170 equivalent mobile and immobile fractions (0.50 ± 0.02; mean ± sem) for the protein Sla2, indicating that
171 mobile fractions of Sla2 proteins are able to exchange with their surroundings on time scales of tens of
172 seconds (Fig. 2*C*).
173
174 **PLDs are necessary for the formation of functional endocytic condensates.** Next, we explored whether
175 endocytic condensates formed by PLD-containing proteins require their PLDs to associate with the
176 condensates and enable actin-independent endocytosis. Since HD generally disrupts interactions among
177 PLD-containing proteins in biomolecular condensates we tested whether dissolution of Sla1-labeled puncta
178 with HD inhibited both actin-dependent and independent endocytosis in *GPD1Δ* cells as quantified by the
179 uptake of the external fluid-phase (Measured by Lucifer Yellow (LY) uptake) and membrane components
180 (Measured by FM4-64 uptake), respectively (Fig. 3*A, B*). Dissolution by HD (concentration of 5% wt/v)
181 led to inhibition of the uptake of membrane components. The HD concentration we used is considerably
182 lower than the concentration necessary to disrupt membrane or Syp1-labeled cortical patch structures (Fig.
183 3*B*, *SI Appendix*, S3 *B-E*). Importantly, the inhibitory effect of HD on endocytosis was independent of
184 turgor pressure or actin polymerization (Fig. 3*A* and *SI Appendix*, Fig. S5).
185
186 Next, we tested the specific importance of PLDs in endocytosis. For this, we tested whether specific
187 PLDs are required for the assembly of endocytic condensates and actin-independent endocytosis. Deletion
188 of the PLDs of Sla1 and Ent1 caused mis-localization of the Sla1, Ent1, Ent2, Yap1801 or Yap1802 proteins
189 and also impaired endocytosis for Sla1 or Ent1 with their PLDs deleted (Fig. 3 *C-D*). These observations
190 were consistent with previous reports regarding the effects of deletion mutants of Sla1 and Ent1 (Warren,
191 Andrews et al. 2002, Mukherjee, Coon et al. 2009). Recruitment of Ent2, Yap1801 and Yap1802 to
192 endocytic condensates required their PLDs but were not essential to endocytosis, though they may serve
193 other roles in regulating endocytosis.
194
195 **The interaction network within endocytic puncta is governed by sequence features of PLDs.**
196 Recent studies have shown that multicomponent biomolecular condensates such as stress granules are
197 governed by a core macromolecular network with an uneven distribution of interactions across nodes of the
198 network (Sanders, Kedersha et al. 2020, Yang, Mathieu et al. 2020). Such networks are wired by specific
199 types of network motifs or features. The functional importance of Sla1 and Ent1 and their PLDs suggests
200 that they play the roles of scaffolds in organizing endocytic condensates (Kukulski, Schorb et al. 2012, Wei,
201 Elbaum-Garfinkle et al. 2017, Alberti, Saha et al. 2018). To probe the organization of the protein-protein
202 interaction network that underlies endocytic condensates, we performed an *in vivo* screen for protein-

203 protein interactions. Specifically, we used a Protein-fragment Complementation Assay with the reporter
204 protein DiHydroFolate Reductase (DHFR PCA) to quantify the effects of PLD deletion on *in vivo*
205 interactions involving or mediated by Sla1 (Fig. 4*A*). Selection for DHFR reconstitution with Sla1 in which
206 the PLD was deleted (*Sla1 ΔPLD)* revealed the preservation of only two out of the thirteen interactions that
207 were detected with the full length Sla1. The interactions that were preserved are relevant only to actin-
208 *dependent* endocytosis (Fig. 4 *B-D*). These results reveal sequence features of the Sla1 PLD that coordinate
209 the network of interactions and organization of endocytic condensates.
210
211 **Glutamine-rich PLDs are required for proteins to partition into endocytic puncta**. Given that the PLD of
212 Sla1 is central to coordinating the network of essential protein-protein interactions, we reasoned
213 that determinants of protein partitioning into endocytic condensates and the interactions among
214 them should depend on the amino acid compositions of their PLDs (Patel, Lee et al. 2015, Boke,
215 Ruer et al. 2016, Alberti, Saha et al. 2018, Wang, Choi et al. 2018, Vijayakumar, Perrois et al.
216 2019). PLDs have distinctive compositional biases that include ratios of Asn *versus* Gln and the
217 uniform sequence distribution of aromatic amino acids (Martin, Holehouse et al. 2020). Alberti *et*
218 *al.,* showed that PLDs that drive the formation of amorphous and insoluble amyloid fibrous bodies
219 have a clear preference for Asn over Gln. Conversely, PLDs with higher Gln:Asn ratios form
220 soluble puncta (Alberti, Halfmann et al. 2009). Sla1, Sla2, and the endocytic epsin proteins Ent1
221 and Ent2 have high Gln and Asn contents with a clear preference for Gln. The Gln:Asn ratios in
222 these PLDs are 2:1 in Sla1, ~5:1 in Sla2, ~3:1 in Ent1, and ~4:1 in Ent2, respectively.
223
224 To test if higher Gln content is essential for partitioning into and the material properties of
225 endocytic condensates, we used artificial PLDs to substitute for the native endocytic PLDs.
226 Specifically, we leveraged the work of Halfmann *et al.,* who compared the prion-forming potential
227 of the NM domain of *wildtype* Sup35 (Sup35 NM), which includes a PLD, to those of Sup35 in
228 which all NM domain Gln residues are substituted for Asn (Sup35 NM (N)) or all Asn substituted
229 with Gln (Sup35 NM (Q)) (Halfmann, Alberti et al. 2011). The Gln:Asn ratios in these PLDs are
230 ~1.5:1 (Sup35 NM), 1:33 (Sup35 NM (N)), and 9:1 (Sup35 NM (Q)). We designed different
231 chimeras of the endocytic epsin proteins Ent1 and Ent2, in which the cognate PLDs within these
232 proteins were replaced with either that of Sla1 or variants of the non-endocytic protein Sup35 NM
233 domain (Fig. 5*A*). Although, the Sla1 PLD shares little sequence identity with either Ent1 or Ent2
234 PLDs (*SI Appendix*, Fig. S6*A, B*), Sla1 PLD chimeras of Ent1 and Ent2 partitioned into endocytic

condensates (Fig. 5*B, C* and S6 *C-G*). Lowering the Gln:Asn ratio or inverting this in favor of Asn increases the amyloid forming potential of PLDs (Halfmann, Alberti et al. 2011). We tested additional Ent1 or Ent2 chimeras wherein the cognate PLDs were replaced with Sup35 NM, NM(N) or NM(Q). We assessed the effects of these substitutions on the partitioning of chimeras into endocytic condensates (Fig. 5*A*). Consistent with the need for a clear asymmetry between the numbers of Gln *versus* Asn, we observed that only the Sup35 NM(Q) chimeras of Ent1 and Ent2 partitioned into Sla1-labeled endocytic condensates (Fig. 5*E*, *SI Appendix*, S6*F, G*). Conversely, the Sup35 NM and Sup35 NM(N) chimeras did not partition into endocytic condensates; instead, they formed distinct puncta, indicative of structural features and interaction preferences that are distinct from those of endocytic condensates (Fig. 5*E, G*). We further surmised that the fibrillar content of Sla1 labeled puncta must be low; to test this hypothesis, we measured the staining of Sla1 labeled endocytic condensates using Thioflavin (ThT), which is a marker for amyloid-like aggregates (*SI Appendix*, Fig. S6*H, I*) (Alberti, Saha et al. 2018, Wang, Choi et al. 2018). These data showed an absence of ThT staining in Sla1-labeled endocytic condensates or in puncta formed by Sup35 NM(Q) (Halfmann, Alberti et al. 2011).

Our data show that the compositional features of PLDs, particularly the asymmetry between numbers of Gln *versus* Asn, are essential for defining the selective partitioning of proteins into endocytic condensates. In addition, the human orthologs of epsins, EPN1 and EPN3 expressed in yeast did not partition into Sla1-labeled endocytic puncta (Fig. 5*D* and *SI Appendix*, S6 *C-E*). Among the human chimeric proteins that we generated, only the Sla1 PLD chimera of EPN1 partitioned to endocytic puncta, whereas all other chimeras did form independent puncta (Fig. 5*D*, *F, G*). These data point to a clear preference for Gln-rich, non-amyloid forming PLDs derived from yeast, which have different compositional biases than proteins with PLDs from other organisms. It is also worth noting that even if several PLDs share generic physical properties that result in their partitioning into the same biomolecular condensates, each resulting condensate does not have the same material properties (Wang, Choi et al. 2018). This is important because material properties of endocytic condensates could tune to their mechano-active potentials. Consistent with this view, among all of the PLD chimeras of Ent1, including those that did partition to endocytic condensates, only the Sla1 chimera supported endocytosis as measured by FM4-64 dye uptake in *ENT1*Δ cells (Fig. 5*H*).

266

267

268 **Discussion**

269

270 We have presented data to show that endocytic condensates form at cortical sites and these
271 hemispheric bodies require cohesive interactions provided by PLDs within endocytic coat proteins.
272 Endocytic condensates form reversibly, and they are required to drive clathrin- and actin-independent
273 endocytosis. How might condensates contribute to endocytosis in the absence of actin? Several mechanisms
274 could act in synergy with the formation of the endocytic condensates to drive mechanical invagination of
275 the plasma membrane. These include (a), contributions from membrane curvature-inducing proteins and
276 protein complexes, including convex-shaped BAR (for Bin, Amphiphysin and Rvs) domain-containing
277 proteins (Youn, Friesen et al. 2010, Yu and Schulten), (b) insertion of an amphipathic helix into the outer
278 leaflet of the membrane bilayer, which pushes the head groups apart (Ford, Mills et al. 2002, Boucrot, Pick
279 et al. 2012), (c) modulation of lipid composition (Graham and Kozlov 2010, Anitei, Stange et al. 2017), (d)
280 local relief of turgor pressure (Scher-Zagier and Carlsson 2016) and (e) "steric pressure" exerted at cortical
281 sites due the excluded volumes of proteins that encompass certain categories of disordered domains (Busch,
282 Houser et al. 2015, Snead, Hayden et al. 2017). Finally, analogous to condensates formed by synthetic
283 polymers that are known to drive membrane vesicle formation from artificial phospholipid bilayers (Li,
284 Lipowsky et al. 2011), we postulate that cohesive interactions that contribute to the formation of endocytic
285 condensates also make these condensates mechanoactive by providing the free energy to drive membrane
286 remodeling (Bergeron-Sandoval and Michnick 2018).

287

288 Of the mechanisms enumerated above, two stand out for the distinctive roles that are
289 ascribed to intrinsically disordered regions (IDRs) of proteins, the steric pressure model and our
290 mechanoactive model (Bergeron-Sandoval and Michnick 2018, Yuan, Alimohamadi et al. 2020).
291 Stachowiak and coworkers have proposed that IDRs can drive membrane remodeling and
292 endocytosis primarily via excluded volume effects – a phenomenon they refer to as "steric
293 pressure" (Busch, Houser et al. 2015). Their recent studies also suggest that phase separation of
294 IDRs involved in generating steric pressure also undergo phase separation via depletion-mediated
295 forces (Yuan, Alimohamadi et al. 2020). Of course, not all IDRs adopt expanded conformations
296 with high excluded volumes (Das, Ruff et al. 2015). Instead, IDRs come in different flavors; for
297 instance IDRs such as the PLDs of Sla1, Sla2, Ent1, and Ent2 are deficient in charged or proline

residues and are characterized by cohesive interactions with one another leading to compact conformations with average radii similar to those of folded proteins (Ruff, Pappu et al. 2019). Therefore, there appear to be two distinct categories of IDRs that drive membrane invagination namely those that do so *via* "hard" repulsive interactions afforded by expanded IDRs and a different category of IDRs that drive condensate formation *via* cohesive interactions, as occurs in our mechanoactive model (Bergeron-Sandoval and Michnick 2018). This raises the interesting prospect of synergies between the two curvature generation mechanisms by two distinct classes of IDRs.

We hypothesize that the energy stored with endocytic condensates can be converted into mechanical work to deform the membrane and the cytosol. The mechanics of this process can be described by analogy to a soft viscoelastic and sticky balloon bound to a soft elastic sheet (Movie S1). A balance between binding and the elastic/surface deformation energies is achieved upon membrane invagination. This idea can be captured in a simple phenomenological model where we express the mean-field energy U stored in a condensate as the sum of mechanical strain energy (ϕ term) and work (ψ term), respectively (*SI Appendix*):

$$U = \phi \cdot \delta^{1+\varepsilon} - \psi \cdot \delta \; ; \tag{1}$$

Here, U is a mean-field energy, δ is the invagination depth of both the membrane and cytosol (which are coupled by virtue of conservation of volume of the condensate) and the exponent $\varepsilon > 0$ is determined by the deformation geometry (*SI Appendix*). At equilibrium, $(\partial U/\partial\delta) = 0$, and we expect invagination to balance the two contributions such that the value of δ^* that minimizes the mean-field energy (1) is computed as,

$$\delta^* = \left(\frac{\psi}{\phi\,(1+\varepsilon)} \right)^{\frac{1}{\varepsilon}} \; ; \tag{2}$$

Equation (2) shows that the invagination depth δ is determined by the ratio ψ/ϕ and the deformation geometry that is captured in the exponent ε. The numerical values of ϕ and ψ can be

327 estimated from the dimensions of the condensates as well as the viscoelastic properties of the
328 cytosol, the condensate, and the membrane, respectively (*SI Appendix*).
329
330 To test whether the endocytic condensates have viscoelastic properties that are required to
331 drive membrane invagination we used active rheology to measure the material properties of the
332 cytosol in which endocytic condensates are embedded. Since the endocytic condensates are too
333 small to probe their material properties directly, we inferred their material properties using the
334 contact theory of Hertz (Hertz 1882). This theory relates the elastic moduli of elastic materials in
335 contact with one another through the resulting geometries of their contacting surfaces. We probed
336 the material properties of the yeast cytoplasm with optical tweezers to measure the frequency-
337 dependent amplitude and phase responses of 200 nm diameter polystyrene beads that are
338 embedded in cells (Fig. 6, *SI Appendix*, Fig. S7*G, H*). We used an acousto-optic device to oscillate
339 the position of the optical trap in the specimen plane at frequencies that spanned over four orders
340 of magnitude and measured the displacement of trapped beads from the trap center using back
341 focal plane interferometry (Fig. 6 *A-C*). We quantified the viscoelastic properties of the cytosol
342 surrounding the beads by measuring the phase and amplitude of displacements of beads in response
343 to oscillations of the optical tweezers and calculated the power spectrum of unforced fluctuations
344 of the bead to obtain storage (G′) and loss (G″) moduli as a function of frequency (Fig. 6*B, C* and
345 *SI Appendix*) (Hendricks and Goldman 2017). We used both the dimensions and time-lapse
346 fluorescence imaging of Sla1-labeled puncta to determine that endocytic condensates expand at a
347 rate of 2360 ± 120 nm s^{-1} (*SI Appendix*, Fig. S7*I, J*), corresponding to a stress at ~30 ± 2 Hz. At
348 this timescale, the cytosol is principally elastic with a shear modulus of approximately 20 Pa (Fig.
349 6*C*). We also measured the linear displacement of Sla1-labeled puncta within the confocal volume
350 as a function of time. Membrane invagination occurs at a velocity of 7.4 ± 2.5 nm s^{-1}, and this
351 corresponds to a frequency of 0.1 ± 0.04 Hz (*SI Appendix*, Fig. S7*I, J*). In this regime, the
352 cytoplasm is viscoelastic and mechanically compliant (Fig. 6*C*). The G′ and G″ values we
353 measured here are similar to those of the cytoplasm of adherent mammalian cells (Hendricks,
354 Holzbaur et al. 2012, Guo, Ehrlicher et al. 2013, Guo, Ehrlicher et al. 2014).
355 Based on the parameters obtained from active rheology including the dynamic modulus of the
356 cytoplasm, we were able to determine the material properties of endocytic condensates embedded in the
357 cytoplasm using Hertz theory and measurements of the dimensions of condensates that we determined by

358 super-resolution microscopy (Fig. 2*A*) (Hertz 1882). We used this information to estimate the apparent
359 Young's modulus of endocytic condensates to be 59 Pa, which is on the same order as that of the cytosol
360 at 45 Pa at 1 Hz (Fig. 6*C*, and *SI Appendix*, *Extended Materials and Methods; Eq. 3.7-3.10*). These results
361 are consistent with those obtained for other protein-based elastic materials (Reichheld, Muiznieks et al.
362 2017).
363
364 The Young-Laplace equation yields an estimate of $\gamma_{dc} = 7 \times 10^{-5}$ N•m^{-1} for the interfacial
365 tension at the condensate-cytosol interface. This estimate is based on the pressure difference across
366 the cytosolic interface and the mean curvature of the condensate (*SI Appendix*, *Extended Materials*
367 *and Methods; Eq. 4.6*). It falls within the range of values that have been reported for other protein
368 condensates, including nucleoli and P granules (*SI Appendix*, *Extended Materials and Methods;*
369 *Eq. 4.9*) (Brangwynne, Mitchison et al. 2011, Elbaum-Garfinkle, Kim et al. 2015).
370
371 Using the inferred apparent elastic modulus for the endocytic condensate, we computed the
372 mechanical strain (ϕ) and mechanical work (ψ), respectively as functions of membrane and cytosol
373 invagination δ (Fig. 7*A*, *SI Appendix*, S8 and *Extended Materials and Methods; Eq. 4.25, 4.26*).
374 Our physical framework suggests that the formation of endocytic condensates generates $4.9 \times 10^{-}$
375 ^{18} J (Fig. 7*A* and Table S*4*), which is within the range of the energy required to provide the
376 necessary membrane invagination. Rheology experiments also yield estimates for the energy of
377 deformation that are strikingly similar. This points to a clear route for force generation by
378 condensates that enables membrane invagination, thereby activating membrane constriction and
379 vesicle scission to drive actin-independent endocytosis (Idrissi, Blasco et al. 2012).
380 A mechanical analogy can aid in understanding our model (Fig. 7*B*, *SI Appendix*, Movie
381 S1). Adhesion of the endocytic condensate to the cytosol tends to drive the condensate to maximize
382 the contact surface area between the condensate and the cytosol. Because the condensate is a
383 viscoelastic material, its volume must remain constant. The area of the condensate-cytosol
384 interface is proportional to the square of the radius. Any increase in interfacial area must be
385 compensated by a decrease in volume of the condensate, which varies by the cube of the radius of
386 the condensate. Since the drive to increase the condensate-cytosol contact is symmetrical, the only
387 way that the condensate volume can be reduced, is by invagination of the membrane. This,
388 however, increases the favorable condensate-membrane surface contact, thus acting as a positive

feedback to further drive membrane invagination. The system comes to equilibrium when the viscoelastic properties of the condensate and cytosol prevent further expansion and invagination. This is the point at which scission of a mature endocytic vesicle must occur.

There remains the question of how the geometry of the observed membrane invagination comes about. Evidence from electron and super-resolution fluorescence microscopy indicates that the favored geometry of the membrane is flat with invagination centered in the middle of the endocytic condensate. Such geometries can be explained by a local radial stress gradient generated by adhesion of the viscoelastic condensate to the membrane on one side and the cytosol or the other (Korchagin, Dolbow et al. 2007). Local radial stress gradients can also be generated by asymmetries in local binding of adaptor proteins, or by distinct lipid compositions. Overall, our model and the questions they raise provide the motivation for continued investigation of the details of regulation of endocytosis in eukaryotic cells. Our model also provides motivation for investigating the mechano-active roles of viscoelastic condensates that contribute to vesicle trafficking processes and involve proteins with PLDs (Pietrosemoli, Pancsa et al. 2013).

Acknowledgements

The authors acknowledge support from CIHR grants MOP-GMX-152556 (SWM), the US National Institutes of Health grant R01NS056114 (RVP), the Fonds Québécois de la Recherche sur la Nature et les Technologies (SWM and PF), the US National Science Foundation through grant MCB-1614766 (RVP), NSERC RGPIN/05843-2014 (AJE), CIHR 143327 (AJE), CFI 32749(AJE and AGH), and the Human Frontier Science Program RGP0034/2017 (SWM and RVP). CEC was supported by the National Institute of General Medical Sciences of the National Institutes of Health (NIH) under award T32GM008268. Research in the Keller Lab is supported by National Science Foundation award MCB-1402059 to SLK. We thank Cliff Brangwynne, Julien Berro, David Drubin, Alex Holehouse, Tom Pollard, and Kiersten Ruff for thoughtful discussions and advice on the manuscript; Jackie Vogel for strains; Susan Liebman, Simon Alberti and Randal Halfmann for plasmids; Jacqueline Kowarzyk and Philippe Garneau for technical assistance and Rosa Kaviani for help with FRAP experiments.

Author Contributions

LPBS and SWM designed the research with the assistance of RVP; LPBS performed biological research; LPBS, AJE, RVP and SWM analysed the biological data; CC, CEC and SLK performed and analysed the vesicle leakage experiments; LPBS and HKH performed micro rheology experiments; LPBS, HKH, AJE and AGH analysed micro rheology data; LPBS, HKH and PF developed physical model; LPBS and SWM wrote the first version, all authors corrected the paper.

Competing Interest Statement: RVP is a member of the Scientific Advisory Board of Dewpoint Therapeutics. All other authors declare no competing interests.

Supplementary Materials

Materials and Methods

Figures S1-S6

Tables S1-S4

Movies S1-S2

433 **Figures**

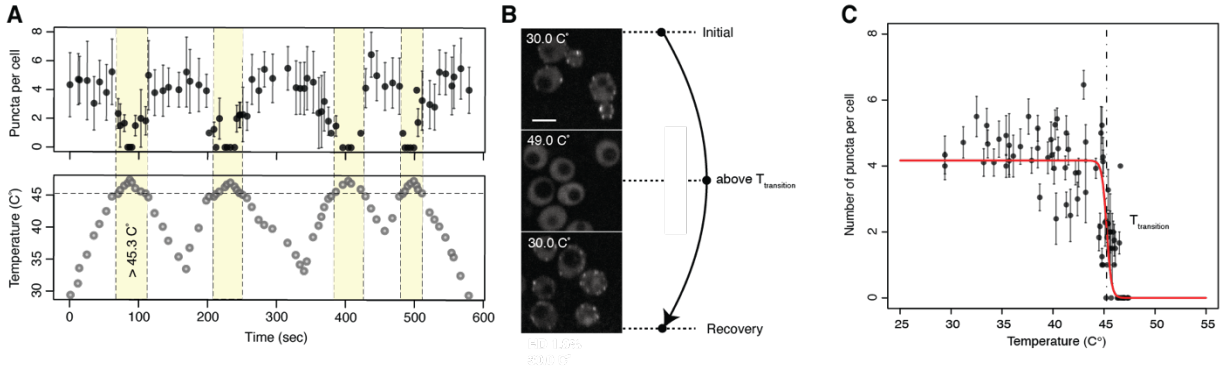

434
435

436 **Figure 1. Endocytic proteins with PLDs form thermo-sensitive puncta.** (A) Reversible, temperature-
437 dependent dissolution and formation of Sla1-labeled endocytic puncta when cells are cycled above
438 and below an apparent transition temperature (T_t) of 45.3 C° (yellow region) over multiple heating
439 and cooling cycles (left; mean ± sd; n > 8 cells). (B) Representative images of temperature-
440 dependent dissolution and reformation of Sla1-labeled endocytic puncta in *GPD1Δ* cells treated
441 with Lat A when cells are cycled above and below a transition temperature (T_t) over a heating and
442 cooling cycle. Scale bar, 4 μm. (C) Average number of puncta per cell is bistable as a function of
443 temperature.

444

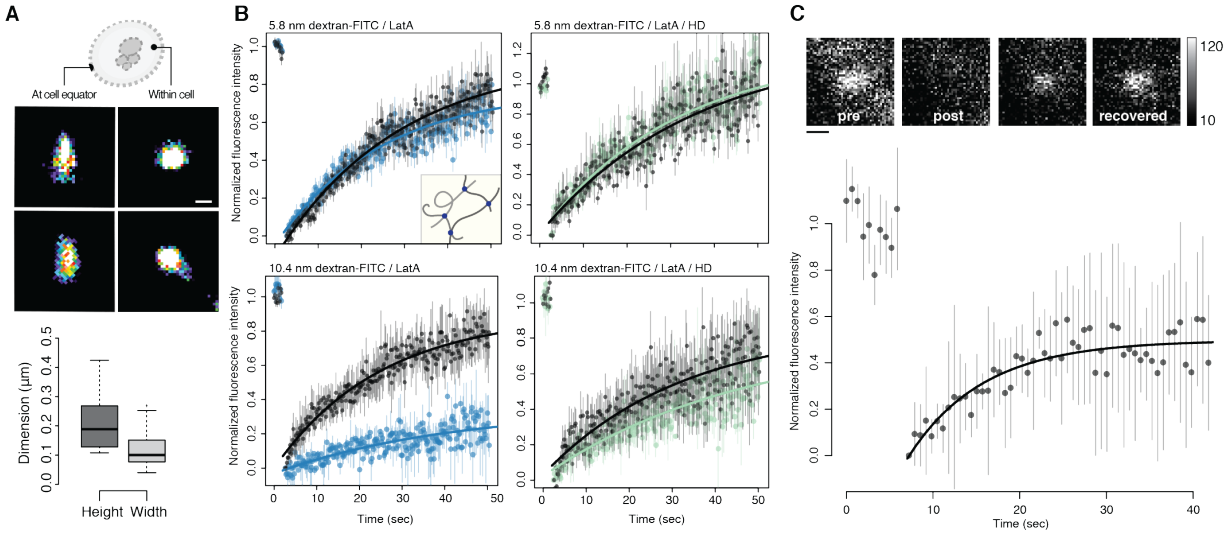

Figure 2. Endocytic puncta form dense condensates of labile molecules. (A) Dimensions of Sla1-GFP-labeled puncta measured using super-resolution microscopy (dSTORM). Lateral x, y resolution was ~10 nm. Pseudo-color reconstructed images show circular structures when viewed from the top, or within cells (top right), and narrow ellipses when imaged at the equator of cells (top left). Automatic segmentation (center) was performed on these images to determine the length (209 ± 10 nm) and width (118 ± 6 nm) of the endocytic puncta (n = 250). (B) Endocytic puncta are dense lattices that exclude molecules having dimensions > 10 nm. Fluorescence recovery after photobleaching (FRAP) of dextran-FITC molecules within endocytic puncta or neighbouring cytosol. FRAP of the bleached 5.8 nm dextran-FITC within either a Sla1-mCherry (top left panel; Lat A treated cells; blue) or a Syp1-mCherry (top right panel; Lat A and 5% HD treated cells; green) puncta and neighbouring cytosol regions (black) without Sla1 or Syp1 signals, respectively. Insert illustrates porous latticework composed of amorphous protein chains (grey filaments) with binding sites (dots) through which they are non-covalently associated. Same experiment with 10.4 nm dextran-FITC that scarcely permeate the Sla1 puncta (bottom left panel; Lat A treated cells; blue) but are mobile when puncta are dissolved by HD (bottom right panel; Lat A and 5% HD treated cells; green). Data points (mean ± SEM; n = 10 cells) were fitted to a single term recovery function (Methods). (C) Coat proteins exchange with endocytic puncta at rates typical of those observed for biomolecular condensate proteins. FRAP of Sla2-GFP: Signal recovery was measured within a segmented Sla1-mCherry region of interest to ensure that FRAP was acquired within the endocytic puncta (mean ± sd; n = 10 cells. Data fitted to a single term exponential, see

467 Materials & Methods). Incomplete fluorescence recovery suggests that endocytic puncta are
468 viscoelastic. Representative foci images (insert) before and upon bleaching and after recovery. 8-
469 bit grayscale values, 10 to 120. Scale bar, 250 nm.
470

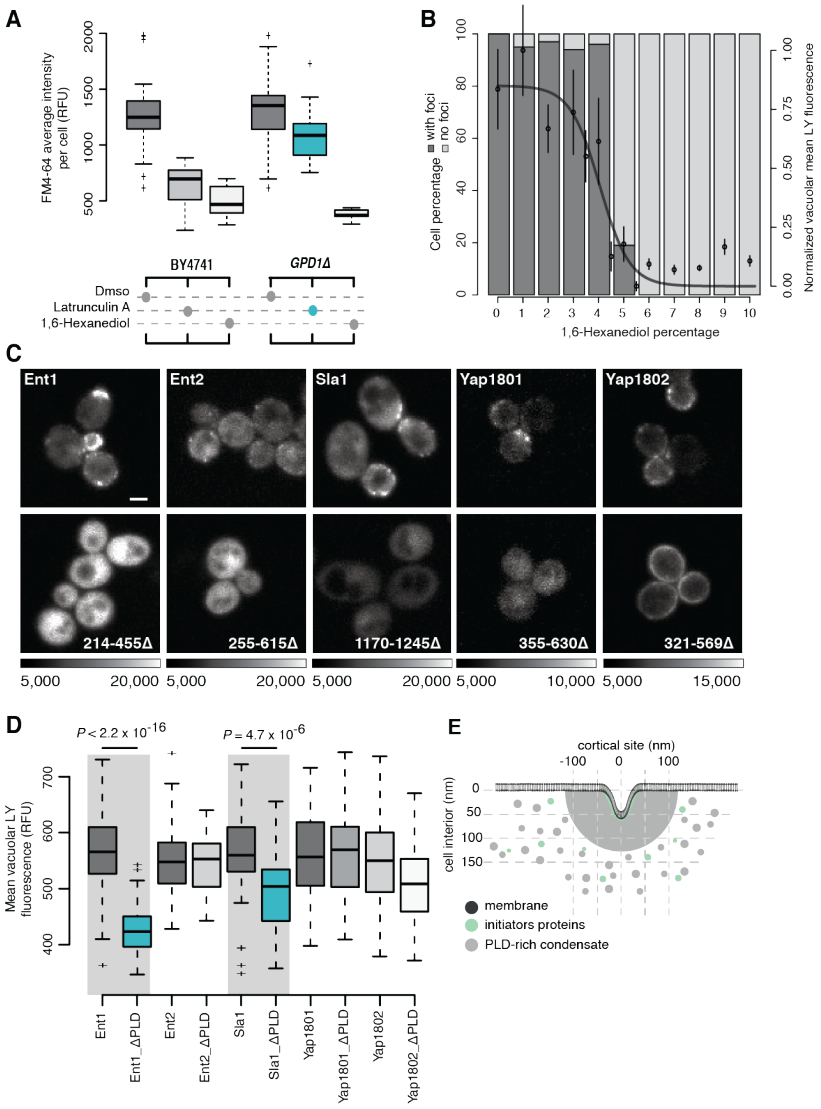

Figure 3. Puncta formed by PLD-containing proteins are necessary for actin-independent endocytosis. (A) Quantification of the membrane uptake of a lipophilic membrane-bound fluorescent dye (FM4-64) in *wildtype* BY4741 (left) and *GPD1*Δ cells (eliminates turgor pressure; right) treated with either DMSO, latrunculin A (prevents F-actin polymerization) or 1,6-hexanediol (Non-specifically alters solvent quality). Each boxplot shows the relative fluorescence units of n = 50 cells. *GPD1*Δ cells can undergo endocytosis in the absence of F-actin polymerization (blue) because there is no turgor pressure in these cells. (B) At fixed temperature, HD dissolves endocytic puncta and this in turn inhibits endocytosis. The bar plot quantifies the percentage of cells that contain Sla1-GFP foci (dark grey), or not (light grey), as a function of HD concentration monitored as counts of endocytic puncta

482 labeled with Sla1-GFP (n = 150 cells). Plot overlay: fluid uptake of water-soluble fluorescent dye
483 Lucifer Yellow (LY) into vacuoles (mean ± sd; n = 25 foci; logistic fit). (C) Prion-like domains
484 (PLDs) of endocytic coat proteins are essential for their localization to endocytic puncta.
485 Fluorescence images of cortical localization of Ent1, Ent2, Sla1, Yap1801 and Yap1802 fused to
486 Venus YFP. Full-length (upper panels) *versus* C-terminal PLD truncation mutants of the proteins
487 (lower panels). Sequence ranges of deleted PLDs indicated (lower) and grayscale dynamic ranges
488 for image pairs. Scale bar, 2 μm. (D) Lucifer yellow dye uptake for strains that express either full-
489 length or PLD deletion mutants of Ent1, Ent2, Yap1801, Yap1802 and Sla1 (as detailed in panel
490 C). Reductions in Ent1 and Sla1 mutants are significant (n = 100 cells; two-sided t-test; see
491 Materials and Methods). (E) Illustration of the membrane topology (dark grey) and remodelling
492 into the cell during endocytosis in the absence of actin. Electron microscopy data suggest that
493 clathrin-coated plasma membrane patches are surrounded by a cortical body of ~200 nm diameter
494 (light grey) before appearance of actin structures (6). Clathrin heavy and light chains (Chc1 and
495 Clc1) interact with initiator proteins (Ede1 and Syp1) to form a lattice on the membrane (in green).
496 Subsequently, PLD-containing coat proteins (light grey), such as Sla1/2, Ent1/2, and Yap1801/2,
497 directly bind to the initiator-clathrin lattice and form the endocytic puncta (in grey).
498

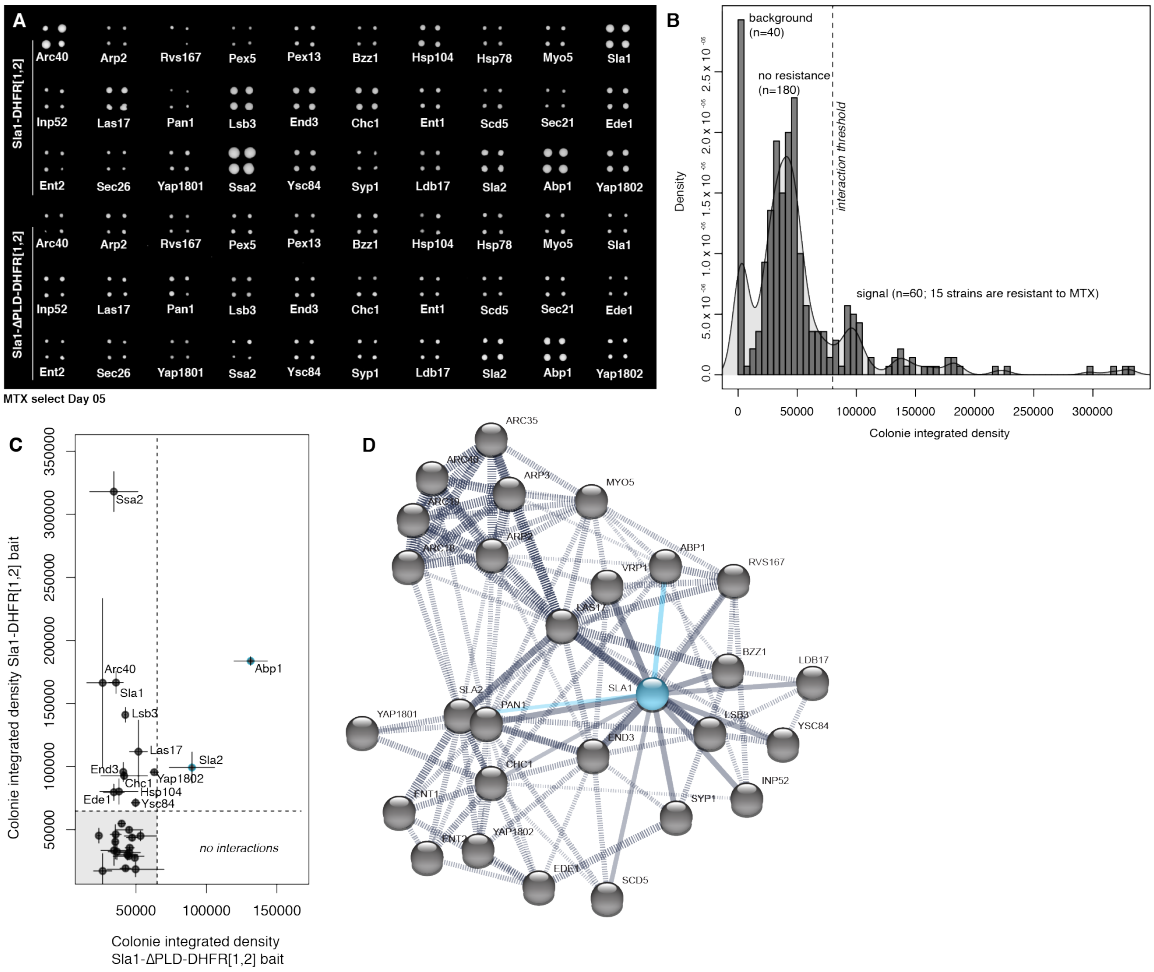

Figure 4. Proteins can partition into endocytic puncta through a network for interactions coordinated by PLDs. (A) DHFR-PCA and methotrexate (MTX) selection plate after 5 days of growth shows that the PLD deletion mutant of Sla1 loses all but two interactions of *wildtype* Sla1. (B) Density (number of colonies with given total pixel intensity) *versus* colony integrated growth (total pixel intensity) after 5 days of MTX selection for DHFR reconstitution. Peaks are labelled with their corresponding measurements for plate background (n=40 empty spots), colonies with no resistance to MTX (n=180 colonies; 45 strains) and colonies that grow on MTX (n=60 colonies; 15 strains) above a selected integrated density threshold. We detected 13 interactions for full-length Sla1 protein. (C) Colony integrated growth (total pixel intensity) after 5 days of MTX selection for DHFR reconstitution with *wildtype* Sla1 *versus* colony integrated growth (total pixel intensity) after 5 days of MTX selection for DHFR reconstitution with PLD deletion mutant of Sla1. Compared to *wildtype* Sla1 interactions, we detect 2 interactions (blue points) for the mutant Sla1 protein that do not contain the PLD. (D) Protein interaction network from STRING (version 11.0)

513 for the selected subarray of 30 potential interactors (grey dots) of Sla1 (blue dot). We represent
514 the 13 direct Sla1 interactions (solid black lines) and DHFR-PCA interactions with Apb1 and Sla2
515 that are preserved with the PLD deletion mutant of Sla1 (solid blue lines) amongst all the protein-
516 protein interactions (dashed black lines) determined experimentally.
517

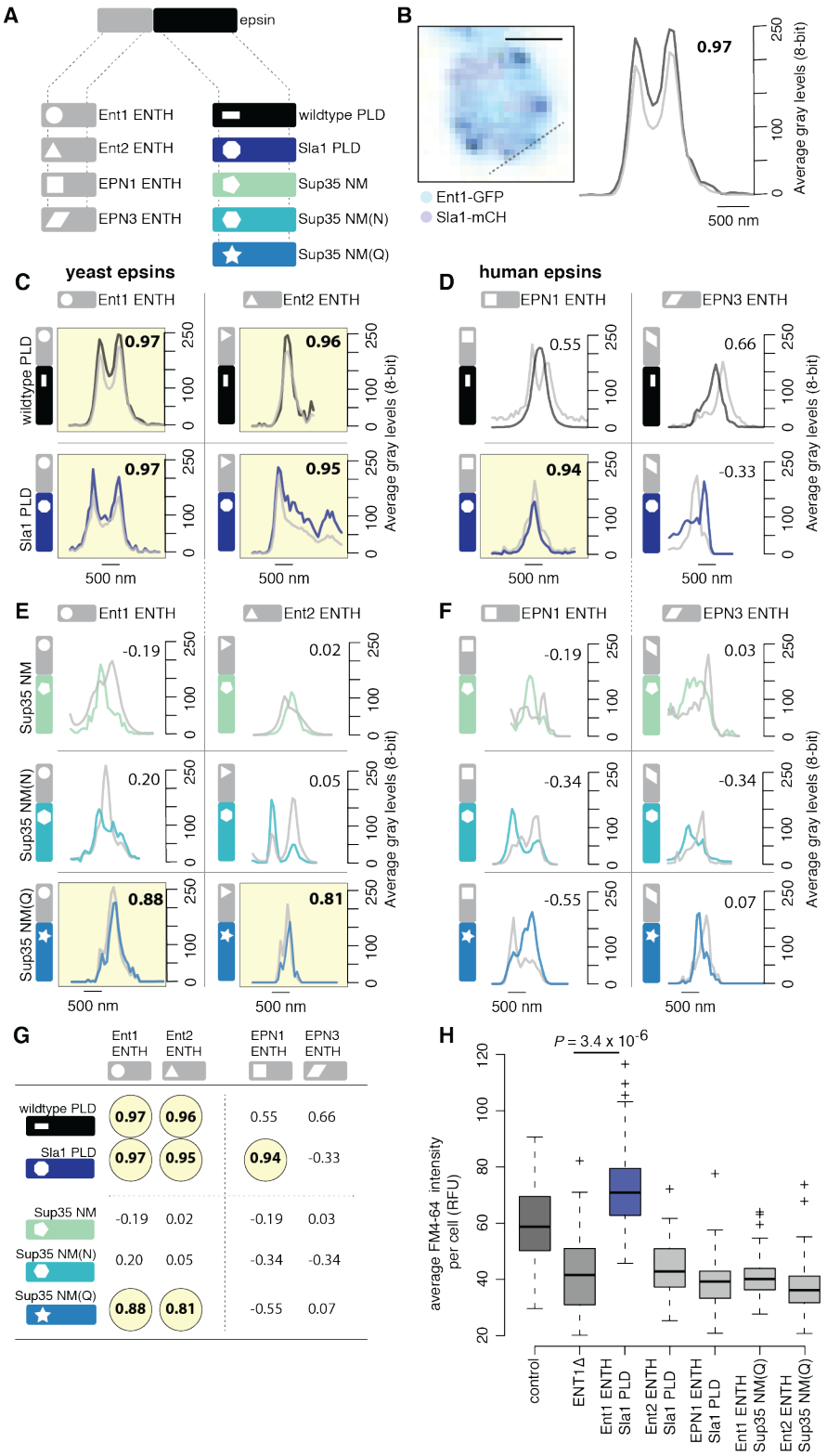

Figure 5. PLDs with shared sequence features can be interoperable and drive assembly of functional endocytic condensates. (A) Illustration of the general structure of epsin proteins (top) with the four ENTH

521 modules (bottom left; shape coded) and five PLD modules (bottom right; colour and shape coded)
522 we used to construct sixteen different protein chimeras. (B) Colocalization of Ent1-GFP signal
523 (black) with signal of Sla1-mCherry labelled endocytic puncta (gray) in yeast cells (left), line scan
524 on confocal fluorescence images (right) was performed as indicated on the cell image (left; dashed
525 line). Pearson correlation values between the fluorescence signals are given (top right of plot) to
526 confirm whether the signals colocalize (values above 0.8 are considered significant and highlighted
527 in yellow in panels C-F; corresponds to a *p-value* < 0.005). Scale bar 1 μM. (C) Wildtype yeast
528 epsin proteins Ent1 and Ent2 (top) and chimeras of Ent1 ENTH and Ent2 ENTH respectively fused
529 to Sla1 PLD (bottom). (D) Wildtype human epsin proteins EPN1 and EPN3 (top) and chimeras of
530 EPN1 ENTH and EPN3 ENTH respectively fused to Sla1 PLD (bottom).
531 (E) Chimeras of Ent1 ENTH and Ent2 ENTH respectively fused to either Sup35 NM (top), Sup35
532 NM(N) (middle) or Sup35 NM(Q) (bottom). (F) Chimeras of human EPN1 ENTH and EPN3
533 ENTH respectively fused to either Sup35 NM (top), Sup35 NM(N) (middle) or Sup35 NM(Q)
534 (bottom). (G) Summary of the Pearson correlation values for colocalization of all wildtype and
535 chimera proteins with endocytic puncta described in C-F with. Values above 0.8 are considered
536 significant and highlighted in yellow, corresponding to a *p-value* < 0.005. (H) FM4-64 dye uptake
537 in cells for strains that overexpress fusions of the yeast Ent1 ENTH, yeast Ent2 ENTH or human
538 EPN1 ENTH respectively fused to either Sla1 PLD or Sup35 NM(Q) that are shown to colocalize
539 with endocytic puncta in C-F (n = 100 cells; two-sided t-test; see *SI Appendix, Extended Materials*
540 *and Methods*).
541

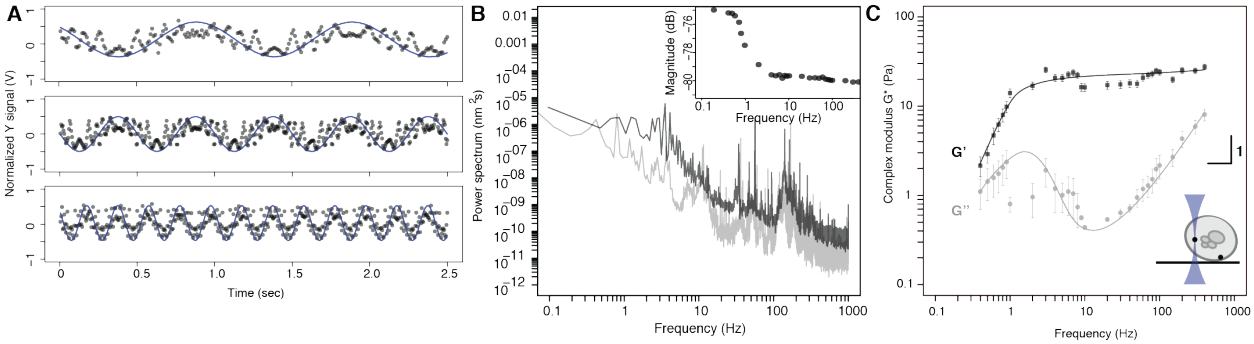

Figure 6. Sla1-labelled condensates are embedded in a viscoelastic cytosol. (D) Position sensitive detector (PSD) output signal in volts (V) *versus* time for acquisitions made at 1Hz (top), 2 Hz (middle) and 5 Hz (bottom). A bead located in the cytoplasm was oscillated with the AOD in the Y-axis of the specimen plane with fixed tweezer movement amplitude (normalized blue curve) at different frequencies. The recorded PSD raw traces (black points) were normalized to a corresponding magnitude range (coherence cutoff of 0.9). (B) Power spectrum of the oscillated bead (black) with magnitude of response as a function of frequency (insert). (C) Decomposition of G* as a function of frequency into G′ (storage modulus; darker squares) and G″ (loss modulus; light shade circles) for beads distributed at both the cell periphery and interior (see schematic insert; mean ± sd; n = 17 cells) with an average trap stiffness k_{trap} (mean ± se; $8.0 \times 10^{-5} \pm 2.7 \times 10^{-5}$ N m^{-1}) and photodiode sensitivity factor β (mean ± se; $10.7 \times 10^{3} \pm 2.3 \times 10^{3}$ nm V^{-1}).

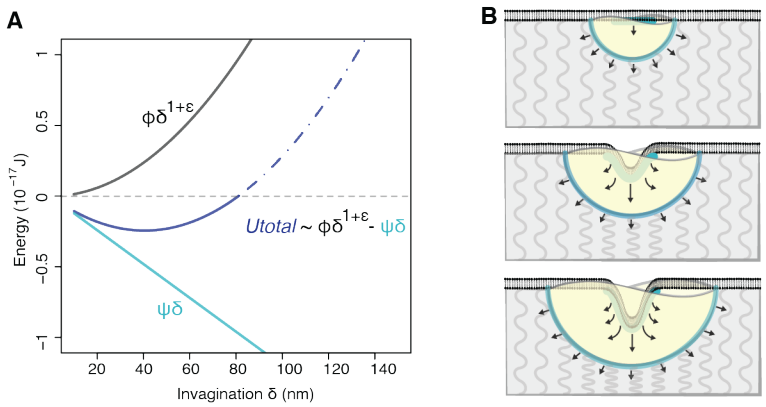

Figure 7. Endocytic condensates do mechanical work to deform the membrane and cytosol. (A) Energy U_{total} *versus* membrane invagination d determined from equation (1), (inset) determined by opposing (ϕ) and favoring (ψ) energy terms. U_{total} (dark blue), ϕ (black) and ψ (light blue) versus δ. The energy is favourable for δ between about 15-80 nm (solid blue line) and unfavorable above 80 nm (dashed blue line). Quantities used to calculate energies are detailed in Fig. S8*A*, Tables S2, S3 and S4. (B) Mechanical description of endocytic condensate-driven membrane invagination. Endocytic condensate (yellow) binds to (wets) the bilayer membrane (black) and drives membrane invagination as the condensate expands to maximize contact with the cytosol (top to bottom). Forces balance under a Young-Dupré adhesion gradient (blue lines and arrows) and resistance of the cytosol (grey curved lines).

References

1. Aghamohammadzadeh, S. and K. R. Ayscough (2009). "Differential requirements for actin during yeast and mammalian endocytosis." Nat Cell Biol **11**(8): 1039-1042.
2. Aghamohammadzadeh, S., R. Smaczynska-de, II and K. R. Ayscough (2014). "An Abp1-dependent route of endocytosis functions when the classical endocytic pathway in yeast is inhibited." PLoS One **9**(7): e103311.
3. Alberti, S., R. Halfmann, O. King, A. Kapila and S. Lindquist (2009). "A systematic survey identifies prions and illuminates sequence features of prionogenic proteins." Cell **137**(1): 146-158.
4. Alberti, S., S. Saha, J. B. Woodruff, T. M. Franzmann, J. Wang and A. A. Hyman (2018). "A User's Guide for Phase Separation Assays with Purified Proteins." Journal of Molecular Biology **430**(23): 4806-4820.
5. Alberti, S., S. Saha, J. B. Woodruff, T. M. Franzmann, J. Wang and A. A. Hyman (2018). "A User's Guide for Phase Separation Assays with Purified Proteins." J Mol Biol **430**(23): 4806-4820.
6. Anitei, M., C. Stange, C. Czupalla, C. Niehage, K. Schuhmann, P. Sala, A. Czogalla, T. Pursche, U. Coskun, A. Shevchenko and B. Hoflack (2017). "Spatiotemporal Control of Lipid Conversion, Actin-Based Mechanical Forces, and Curvature Sensors during Clathrin/AP-1-Coated Vesicle Biogenesis." Cell Rep **20**(9): 2087-2099.
7. Banani, S. F., H. O. Lee, A. A. Hyman and M. K. Rosen (2017). "Biomolecular condensates: organizers of cellular biochemistry." Nat Rev Mol Cell Biol **18**(5): 285-298.
8. Basu, R., E. L. Munteanu and F. Chang (2014). "Role of turgor pressure in endocytosis in fission yeast." Mol Biol Cell **25**(5): 679-687.
9. Bergeron-Sandoval, L. P. and S. W. Michnick (2018). "Mechanics, Structure and Function of Biopolymer Condensates." J Mol Biol **430**(23): 4754-4761.
10. Bergeron-Sandoval, L. P., N. Safaee and S. W. Michnick (2016). "Mechanisms and Consequences of Macromolecular Phase Separation." Cell **165**(5): 1067-1079.
11. Boke, E., M. Ruer, M. Wuhr, M. Coughlin, R. Lemaitre, S. P. Gygi, S. Alberti, D. Drechsel, A. A. Hyman and T. J. Mitchison (2016). "Amyloid-like Self-Assembly of a Cellular Compartment." Cell **166**(3): 637-650.
12. Boucrot, E., A. Pick, G. Camdere, N. Liska, E. Evergren, H. T. McMahon and M. M. Kozlov (2012). "Membrane fission is promoted by insertion of amphipathic helices and is restricted by crescent BAR domains." Cell **149**(1): 124-136.
13. Brangwynne, C. P., T. J. Mitchison and A. A. Hyman (2011). "Active liquid-like behavior of nucleoli determines their size and shape in Xenopus laevis oocytes." Proc Natl Acad Sci U S A **108**(11): 4334-4339.
14. Busch, D. J., J. R. Houser, C. C. Hayden, M. B. Sherman, E. M. Lafer and J. C. Stachowiak (2015). "Intrinsically disordered proteins drive membrane curvature." Nat Commun **6**: 7875.
15. Carlsson, A. E. and P. V. Bayly (2014). "Force generation by endocytic actin patches in budding yeast." Biophys J **106**(8): 1596-1606.
16. da Silva Pedrini, M. R., S. Dupont, A. de Anchieta Camara, Jr., L. Beney and P. Gervais (2014). "Osmoporation: a simple way to internalize hydrophilic molecules into yeast." Appl Microbiol Biotechnol **98**(3): 1271-1280.
17. Das, R. K., K. M. Ruff and R. V. Pappu (2015). "Relating sequence encoded information to form and function of intrinsically disordered proteins." Current opinion in structural biology **32**: 102-112.
18. Derjaguin, B. V., V. M. Muller and Y. P. Toporov (1975). "Effect of contact deformations on the adhesion of particles." Journal of Colloid and Interface Science **53**(2): 314-326.
19. Elbaum-Garfinkle, S., Y. Kim, K. Szczepaniak, C. C. Chen, C. R. Eckmann, S. Myong and C. P. Brangwynne (2015). "The disordered P granule protein LAF-1 drives phase separation into droplets with tunable viscosity and dynamics." Proc Natl Acad Sci U S A **112**(23): 7189-7194.
20. Ford, M. G., I. G. Mills, B. J. Peter, Y. Vallis, G. J. Praefcke, P. R. Evans and H. T. McMahon (2002). "Curvature of clathrin-coated pits driven by epsin." Nature **419**(6905): 361-366.
21. Graham, T. R. and M. M. Kozlov (2010). "Interplay of proteins and lipids in generating membrane curvature." Curr Opin Cell Biol **22**(4): 430-436.
22. Guo, M., A. J. Ehrlicher, M. H. Jensen, M. Renz, J. R. Moore, R. D. Goldman, J. Lippincott-Schwartz, F. C. Mackintosh and D. A. Weitz (2014). "Probing the stochastic, motor-driven properties of the cytoplasm using force spectrum microscopy." Cell **158**(4): 822-832.
23. Guo, M., A. J. Ehrlicher, S. Mahammad, H. Fabich, M. H. Jensen, J. R. Moore, J. J. Fredberg, R. D. Goldman and D. A. Weitz (2013). "The role of vimentin intermediate filaments in cortical and cytoplasmic mechanics." Biophys J **105**(7): 1562-1568.

24. Halfmann, R., S. Alberti, R. Krishnan, N. Lyle, C. W. O'Donnell, O. D. King, B. Berger, R. V. Pappu and S. Lindquist (2011). "Opposing effects of glutamine and asparagine govern prion formation by intrinsically disordered proteins." Mol Cell **43**(1): 72-84.
25. Hendricks, A. G. and Y. E. Goldman (2017). "Measuring Molecular Forces Using Calibrated Optical Tweezers in Living Cells." Methods Mol Biol **1486**: 537-552.
26. Hendricks, A. G., E. L. Holzbaur and Y. E. Goldman (2012). "Force measurements on cargoes in living cells reveal collective dynamics of microtubule motors." Proc Natl Acad Sci U S A **109**(45): 18447-18452.
27. Hertz, H. (1881). "On the contact of elastic solids." Z. Reine Angew. Mathematik **92**: 156-171.
28. Hertz, H. R. (1882). Ueber die Beruehrung elastischer Koerper (On Contact Between Elastic Bodies). Leipzig, Germany, 1895.
29. Idrissi, F. Z., A. Blasco, A. Espinal and M. I. Geli (2012). "Ultrastructural dynamics of proteins involved in endocytic budding." Proc Natl Acad Sci U S A **109**(39): E2587-2594.
30. Kaksonen, M., C. P. Toret and D. G. Drubin (2005). "A modular design for the clathrin- and actin-mediated endocytosis machinery." Cell **123**(2): 305-320.
31. Korchagin, V., J. Dolbow and D. Stepp (2007). "A theory of amorphous viscoelastic solids undergoing finite deformations with application to hydrogels." International Journal of Solids and Structures **44**(11): 3973-3997.
32. Kroschwald, S., S. Maharana, D. Mateju, L. Malinovska, E. Nuske, I. Poser, D. Richter and S. Alberti (2015). "Promiscuous interactions and protein disaggregases determine the material state of stress-inducible RNP granules." Elife **4**: e06807.
33. Kukulski, W., M. Schorb, M. Kaksonen and J. A. Briggs (2012). "Plasma membrane reshaping during endocytosis is revealed by time-resolved electron tomography." Cell **150**(3): 508-520.
34. Li, Y., R. Lipowsky and R. Dimova (2011). "Membrane nanotubes induced by aqueous phase separation and stabilized by spontaneous curvature." Proc Natl Acad Sci U S A **108**(12): 4731-4736.
35. Malinovska, L., S. Kroschwald and S. Alberti (2013). "Protein disorder, prion propensities, and self-organizing macromolecular collectives." Biochim Biophys Acta **1834**(5): 918-931.
36. Martin, E. W., A. S. Holehouse, I. Peran, M. Farag, J. J. Incicco, A. Bremer, C. R. Grace, A. Soranno, R. V. Pappu and T. Mittag (2020). "Valence and patterning of aromatic residues determine the phase behavior of prion-like domains." Science **367**(6478): 694.
37. Martin, E. W., A. S. Holehouse, I. Peran, M. Farag, J. J. Incicco, A. Bremer, C. R. Grace, A. Soranno, R. V. Pappu and T. Mittag (2020). "Valence and patterning of aromatic residues determine the phase behavior of prion-like domains." Science **367**(6478): 694-699.
38. Mukherjee, D., B. G. Coon, D. F. Edwards, 3rd, C. B. Hanna, S. A. Longhi, J. M. McCaffery, B. Wendland, L. A. Retegui, E. Bi and R. C. Aguilar (2009). "The yeast endocytic protein Epsin 2 functions in a cell-division signaling pathway." J Cell Sci **122**(Pt 14): 2453-2463.
39. Münchow, G., F. Schönfeld, S. Hardt and K. Graf (2008). "Protein Diffusion Across the Interface in Aqueous Two-Phase Systems." Langmuir **24**(16): 8547-8553.
40. Mund, M., J. A. van der Beek, J. Deschamps, S. Dmitrieff, P. Hoess, J. L. Monster, A. Picco, F. Nedelec, M. Kaksonen and J. Ries (2018). "Systematic Nanoscale Analysis of Endocytosis Links Efficient Vesicle Formation to Patterned Actin Nucleation." Cell **174**(4): 884-896 e817.
41. Patel, A., H. O. Lee, L. Jawerth, S. Maharana, M. Jahnel, M. Y. Hein, S. Stoynov, J. Mahamid, S. Saha, T. M. Franzmann, A. Pozniakovski, I. Poser, N. Maghelli, L. A. Royer, M. Weigert, E. W. Myers, S. Grill, D. Drechsel, A. A. Hyman and S. Alberti (2015). "A Liquid-to-Solid Phase Transition of the ALS Protein FUS Accelerated by Disease Mutation." Cell **162**(5): 1066-1077.
42. Pietrosemoli, N., R. Pancsa and P. Tompa (2013). "Structural disorder provides increased adaptability for vesicle trafficking pathways." PLoS Comput Biol **9**(7): e1003144.
43. Popov, V. L., R. Pohrt and Q. Li (2017). "Strength of adhesive contacts: Influence of contact geometry and material gradients." Friction **5**(3): 308-325.
44. Powers, S. K., A. S. Holehouse, D. A. Korasick, K. H. Schreiber, N. M. Clark, H. Jing, R. Emenecker, S. Han, E. Tycksen, I. Hwang, R. Sozzani, J. M. Jez, R. V. Pappu and L. C. Strader (2019). "Nucleo-cytoplasmic Partitioning of ARF Proteins Controls Auxin Responses in Arabidopsis thaliana." Mol Cell **76**(1): 177-190 e175.
45. Rayermann, S. P., G. E. Rayermann, C. E. Cornell, A. J. Merz and S. L. Keller (2017). "Hallmarks of Reversible Separation of Living, Unperturbed Cell Membranes into Two Liquid Phases." Biophys J **113**(11): 2425-2432.
46. Reichheld, S. E., L. D. Muiznieks, F. W. Keeley and S. Sharpe (2017). "Direct observation of structure and

dynamics during phase separation of an elastomeric protein." Proc Natl Acad Sci U S A **114**(22): E4408-E4415.

47. Rog, O., S. Köhler and A. F. Dernburg (2017). "The synaptonemal complex has liquid crystalline properties and spatially regulates meiotic recombination factors." eLife **6**: e21455.
48. Ruff, K. M., R. V. Pappu and A. S. Holehouse (2019). "Conformational preferences and phase behavior of intrinsically disordered low complexity sequences: insights from multiscale simulations." Curr Opin Struct Biol **56**: 1-10.
49. Ruff, K. M., S. Roberts, A. Chilkoti and R. V. Pappu (2018). "Advances in understanding stimulus-responsive phase behavior of intrinsically disordered protein polymers." Journal of molecular biology **430**(23): 4619-4635.
50. Sanders, D. W., N. Kedersha, D. S. W. Lee, A. R. Strom, V. Drake, J. A. Riback, D. Bracha, J. M. Eeftens, A. Iwanicki, A. Wang, M. T. Wei, G. Whitney, S. M. Lyons, P. Anderson, W. M. Jacobs, P. Ivanov and C. P. Brangwynne (2020). "Competing Protein-RNA Interaction Networks Control Multiphase Intracellular Organization." Cell **181**(2): 306-324 e328.
51. Scher-Zagier, J. K. and A. E. Carlsson (2016). "Local Turgor Pressure Reduction via Channel Clustering." Biophys J **111**(12): 2747-2756.
52. Snead, W. T., C. C. Hayden, A. K. Gadok, C. Zhao, E. M. Lafer, P. Rangamani and J. C. Stachowiak (2017). "Membrane fission by protein crowding." Proc Natl Acad Sci U S A **114**(16): E3258-E3267.
53. Updike, D. L., S. J. Hachey, J. Kreher and S. Strome (2011). "P granules extend the nuclear pore complex environment in the C. elegans germ line." J Cell Biol **192**(6): 939-948.
54. Vijayakumar, J., C. Perrois, M. Heim, L. Bousset, S. Alberti and F. Besse (2019). "The prion-like domain of Drosophila Imp promotes axonal transport of RNP granules in vivo." Nat Commun **10**(1): 2593.
55. Wang, J., J. M. Choi, A. S. Holehouse, H. O. Lee, X. Zhang, M. Jahnel, S. Maharana, R. Lemaitre, A. Pozniakovsky, D. Drechsel, I. Poser, R. V. Pappu, S. Alberti and A. A. Hyman (2018). "A Molecular Grammar Governing the Driving Forces for Phase Separation of Prion-like RNA Binding Proteins." Cell **174**(3): 688-699 e616.
56. Warren, D. T., P. D. Andrews, C. W. Gourlay and K. R. Ayscough (2002). "Sla1p couples the yeast endocytic machinery to proteins regulating actin dynamics." J Cell Sci **115**(Pt 8): 1703-1715.
57. Wei, M. T., S. Elbaum-Garfinkle, A. S. Holehouse, C. C. Chen, M. Feric, C. B. Arnold, R. D. Priestley, R. V. Pappu and C. P. Brangwynne (2017). "Phase behaviour of disordered proteins underlying low density and high permeability of liquid organelles." Nat Chem **9**(11): 1118-1125.
58. Yang, P., C. Mathieu, R. M. Kolaitis, P. Zhang, J. Messing, U. Yurtsever, Z. Yang, J. Wu, Y. Li, Q. Pan, J. Yu, E. W. Martin, T. Mittag, H. J. Kim and J. P. Taylor (2020). "G3BP1 Is a Tunable Switch that Triggers Phase Separation to Assemble Stress Granules." Cell **181**(2): 325-345 e328.
59. Youn, J. Y., H. Friesen, T. Kishimoto, W. M. Henne, C. F. Kurat, W. Ye, D. F. Ceccarelli, F. Sicheri, S. D. Kohlwein, H. T. McMahon and B. J. Andrews (2010). "Dissecting BAR domain function in the yeast Amphiphysins Rvs161 and Rvs167 during endocytosis." Mol Biol Cell **21**(17): 3054-3069.
60. Yu, H. and K. Schulten (2013). "Membrane sculpting by F-BAR domains studied by molecular dynamics simulations." PLoS Comput Biol **9**(1): e1002892.
61. Yuan, F., H. Alimohamadi, B. Bakka, A. N. Trementozzi, N. L. Fawzi, P. Rangamani and J. C. Stachowiak (2020). "Membrane bending by protein phase separation." bioRxiv: 2020.2005.2021.109751.